

Structural and Aerodynamic Models for Aeroelastic Analysis of Corrugated Morphing Wings

Natsuki Tsushima¹

Japan Aerospace Exploration Agency, Mitaka, Tokyo, 181-0015, Japan

Kensuke Soneda², Tomohiro Yokozeki³, Tato Imamura⁴
The University of Tokyo, Hongo, Tokyo, 113-8656, Japan

Hitoshi Arizono⁵

Japan Aerospace Exploration Agency, Mitaka, Tokyo, 181-0015, Japan

Weihua Su⁶

The University of Alabama, Tuscaloosa, AL, 35487-0280, USA

Two different aeroelastic analysis frameworks with different fidelities for morphing wings with corrugated structures are presented in the paper. One uses a corotational shell finite element method and unsteady vortex-lattice aerodynamic loads to simulate aeroelastic behaviors of morphing wings involving large deformation. The other couples a nonlinear beam theory and a CFD code for aeroelastic analysis. Numerical studies are carried out to evaluate differences in individual structural and aerodynamic solutions of the two different frameworks. Aeroelastic characteristics of corrugated morphing wings are then evaluated using the framework which can consider three-dimensional effects. The feasibility and capability of such a morphing wing with a corrugated structure to achieve wing morphing under aerodynamic loads are also demonstrated. This work allows to understand the aeroelastic characteristics of composite and corrugated wings and assess feasible domains of the methodologies to simulate such morphing wings numerically.

I. Introduction

RECENTLY, wing morphing has generated a good deal of attention as a potential technique to improve aircraft performance and to facilitate economic flight. The morphing technique can achieve the optimal flight performance in a wide range of operation conditions by adaptively changing the wing shape, even in flight conditions in which conventional control surfaces decrease their performance. Specifically, the morphing technology may improve aerodynamic characteristics and reduce structural weight and acoustic noise of aircraft [1-4]. In addition, it may help to improve flight safety through enhancement of stall characteristics and gust alleviation.

The increasing population of global transportation and tighter economic restrictions contribute to the demand for improvements in aircraft performance. This demand has led aircraft engineers to environment-friendly design with low fuel consumption. Previously, as technologies to reduce fuel consumption, improvement of aerodynamic performance and weight reduction by enhancing the traditional wing design and integrating composite materials have been achieved. However, the development of the traditional design has been matured, and other technologies that may bring revolutionary changes to aircraft structures are strongly desired.

¹ Researcher (tsushima.natsuki@jaxa.jp), Aeronautical Technology Directorate, Student Member AIAA.

² Student (soneda@aastr.t.u-tokyo.ac.jp), Dept. of Aeronautics and Astronautics, Member AIAA.

³ Associate Professor (yokozeki@aastr.t.u-tokyo.ac.jp), Dept. of Aeronautics and Astronautics, Member AIAA.

⁴ Associate Professor (imamura@g.ecc.u-tokyo.ac.jp), Dept. of Aeronautics and Astronautics, Member AIAA.

⁵ Associate Senior Researcher (arizono.hitoshi@jaxa.jp), Aeronautical Technology Directorate, Senior Member AIAA.

⁶ Associate Professor (suw@eng.ua.edu), Dept. of Aerospace Engineering and Mechanics, Senior Member AIAA.

Many researchers have studied various technologies to evaluate the performance of morphing wings. One of the contemporary concepts taking advantage of such wing morphing technique is the Variable Camber Continuous Trailing Edge Flap (VCCTEF) system [4, 5]. The VCCTEF adopted a flap system that was capable of changing flap angles in spanwise direction seamlessly. In addition, the system implemented three discrete control surface sections in the chordwise direction contributing to distribute chordwise aerodynamic pressures smoothly. The performance of the VCCTEF system was evaluated based on aerodynamic numerical simulations and wind tunnel tests, and the results showed performance improvements with respect to drag reduction and high-lift up to 6.31%.

Examples of morphing wing technologies include conceptual designs utilizing auxetic or compliant materials/structures corresponding to recent developments in structures and materials technologies. For instance, a morphing wingtip for a regional jet was designed and evaluated by advantageously using the morphing concept and chiral-type auxetic structure [6]. The adaptive wingtip with the chiral structure can be actuated by rotating each node with a torsional actuation. The reduction in fuel consumption over the considered mission profile up to 2% owing to the designed morphing wingtip has been proven in their study. At the same time, a distributedly actuated morphing wing concept was designed and experimentally demonstrated [7]. A continuous variable camber on the trailing edge was achieved with cross-shaped flexible honeycombs with overlying silicone facesheets. A distributed actuation was implemented by a series of pressurized telescopic tube actuators. Their experimental and analytical investigations on the conceptual wing demonstrated the designed trailing edge morphing. Wing morphing technique can be applied not only on the trailing edge, but also the leading edge. A droop-nose morphing wing tip design was studied and tested with compliant structures as a part of European project NOVEMOR (Novel Air Vehicle Configurations: From Fluttering Wings to Morphing Flight) [8]. The compliant droop-nose morphing device consisted of a fiberglass composite skin and topologically optimized compliant mechanisms. Their experiments showed a successful shape change of the morphing device with a reasonable agreement with their numerical analysis results. In the same NOVEMOR project, wing tunnel tests of a compliant morphing wing were also carried out [9]. The wing model had morphing leading and trailing edges based on compliant structures. The compliant morphing wing provided an adequate accuracy in morphing deformation compared with the predicted one obtained from their numerical simulations. Their wind tunnel experiments also proved the potential benefits in the aerodynamic performance. Another concept of morphing wing uses smart materials such as piezoelectric materials. Such piezoelectric-based morphing wings have the two advantages of fast response and high bandwidth. Morphing wings with piezoelectric materials are suitable to suppress aeroelastic instabilities and can extend the flight envelope [10, 11]. In addition, the piezoelectric materials, which convert energies between mechanical and electrical forms, can also provide additional energy from wing vibrations [12]. More recently, spanwise adaptive wings using shape memory alloy (SMA) actuators for Prototype-Technology Evaluation Research Aircraft (PTERA) was developed [13]. Flight tests of the aircraft demonstrated a capability of adaptive wing actuation with the smart materials in flight. However, a better understanding and properly designed actuation mechanism are needed to achieve the practical and efficient application of such innovative aircraft with smart materials.

At the same time, another morphing wing strategy using a simple wiring actuation mechanism with corrugated structures has been studied [14, 15]. Due to the anisotropy, corrugated structures are stiffer in one direction and softer in another direction. The dual functions of a morphing wing, including spanwise load-bearing and chordwise morphing, are therefore possible by taking advantage of the extremely anisotropic property of corrugated structures. One advantage of the corrugated morphing scheme is that it is easy to fabricate corrugated structures. Additionally, corrugated structures can be conveniently actuated with commercially available actuators and wires although other driving methods may also be adopted. Improvement of aerodynamic characteristics and adaptivity to the flight condition with the corrugated-based camber morphing should be adequately evaluated. Energy to drive such wings also needs to be investigated.

Morphing technology aims to very efficient aerodynamic and structural designs (configuration) during flight, contributing to the high performance of aircraft. The morphing wing actively changes its geometry during flight and may undergo large deformations, but small strains, resulting in nonlinear problems such as geometrically nonlinear deformations and limit-cycle oscillations (LCOs). Hence, to analyze morphing aircraft/wings accurately, an aeroelastic model to consider the geometrical nonlinearities is required. The geometrical nonlinearity of highly flexible structures can be considered in different ways. One approach is to use nonlinear beam models [16, 17]. This approach allows for cost-efficient considerations of the geometrical nonlinearity. Another approach is to use nonlinear shell models [18, 19]. The shell models can provide higher accuracy, particularly in case of studying camber morphing concepts having large deformations in the camber. At the same time, there are variations in an aerodynamic model coupled with a structural model for aeroelastic analysis. Even though the accurate nonlinear aeroelastic analysis can be performed by using computational fluid dynamics (CFD) [20, 21], it compromises computational efficiency, especially in case the large wing motion is involved. As an alternative approach, an

unsteady aerodynamic model can be coupled with a geometrically nonlinear finite element model for computational efficiency with adequately accurate solutions, which can be used for preliminary to middle stage of developments. Especially among different aerodynamic models used for problems subjected to large deformations, an unsteady vortex-lattice method has shown to provide simplicity for implementation and computational cost reduction [22, 23].

Although shell finite element methods can provide higher structural fidelity, beam formulations are still widely used in aeroelastic evaluations of wings involving large deformations. In aerodynamic load calculations, the UVLM is used for medium-fidelity analysis with low computational cost, while CFDs are used for higher fidelity analysis. This paper presents two different aeroelastic formulations for morphing wings providing different fidelities. One of the formulations uses a 2-D beam's highly flexible structure (HFS) equation [24] coupled with XFOIL [25] or a CFD code "UTCart" developed by Rinoie & Imamura Laboratory of the University of Tokyo [26-28]. The other couples a co-rotational shell formulation [19] with the unsteady vortex-lattice method (UVLM) to calculate aerodynamic loads [29]. In both formulations, a homogenization method for corrugated structures is integrated into their structural models so that morphing wings with composite corrugated structures can be simulated. In addition, the numerical results obtained by the two aeroelastic formulations are compared with respect to structural and aerodynamic characteristics. Each aeroelastic formulations is evaluated based on the comparisons in terms of their accuracies. Finally, the feasibility and capability of a morphing wing with a corrugated structure are demonstrated using the 3-D aeroelastic framework. The aeroelastic characteristics of the morphing wing is also evaluated.

II. Theoretical Formulation

In this section, two aeroelastic frameworks considering the geometrical nonlinearity are introduced. The first formulation uses a corotational shell finite element method, while a second implemented a beam theory. To properly describe wing morphing by corrugated structures, a corrugated panel model is implemented in both formulations. Moreover, the first formulation uses the vortex-lattice method (UVLM), and the second uses XFOIL or a CFD code "UTCart" for aerodynamic load calculations. The first aeroelastic framework has been validated in the previous works and the full description can be found Ref. [19]. The second aeroelastic framework was fully described in Ref. [17].

A. Structural Model with Corotational Shell Finite Element Method

To describe dynamics of aircraft undergoing large translational and rotational motion during flights, one can define a few coordinate systems, such as the global frame G , the body frame B , and the local beam frame w . These reference frames and coordinate systems are defined in Fig. 1. Bases of the local frame w are w_x , w_y , and w_z , whose directions are toward the wing tip, the leading edge (LE), and normal to the wing surface, respectively. In addition, another coordinate system to solve aerodynamics for the moving surfaces is defined. Traditionally by using the Cartesian coordinate, the X_a , Y_a , and Z_a axes for the aerodynamics coordinate is defined along the flow direction ($-B_y$), toward the starboard (B_x), and normal to the plane made by the first two axes (B_z).

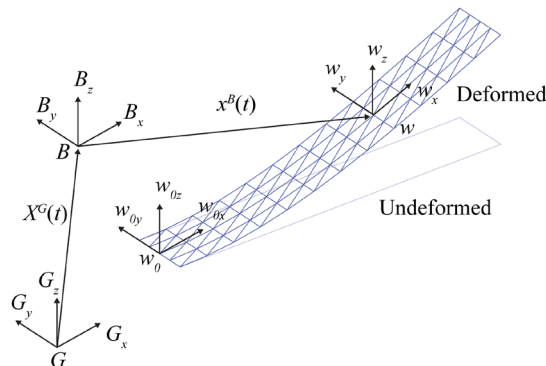


Figure 1. Coordinate systems for the current framework.

The nonlinear structural dynamics is solved using three-node triangular shell element as shown in Fig. 2. The shell element is a superposition of the optimal triangle membrane (OPT) [18, 30] element and discrete Kirchhoff

triangle (DKT) [31] plate bending element. The 18 total degrees of freedom (DOFs) of the triangle shell element are collected in the nodal displacement vector as

$$\begin{Bmatrix} \mathbf{d}_m \\ \mathbf{d}_b \end{Bmatrix} = \begin{Bmatrix} \{u_1 \ v_1 \ \theta_{z1} \ u_2 \ \cdots \ \theta_{z3}\}^T \\ \{w_1 \ \theta_{x1} \ \theta_{y1} \ w_2 \ \cdots \ \theta_{y3}\}^T \end{Bmatrix} \quad (1)$$

and the stiffness matrix of the shell element is

$$[\mathbf{k}]\{\mathbf{d}\} = \begin{bmatrix} [\mathbf{k}_m]_{9 \times 9} & \mathbf{0} \\ \mathbf{0} & [\mathbf{k}_b]_{9 \times 9} \end{bmatrix} \begin{Bmatrix} \{\mathbf{d}_m\} \\ \{\mathbf{d}_b\} \end{Bmatrix} \quad (2)$$

The geometric stiffness is obtained with an integration using seven Gauss points in the area coordinate system as

$$[\mathbf{k}_\sigma] = \int [\mathbf{G}]^T \begin{bmatrix} \bar{\mathbf{N}} & \mathbf{0} & \mathbf{0} \\ \mathbf{0} & \bar{\mathbf{N}} & \mathbf{0} \\ \mathbf{0} & \mathbf{0} & \bar{\mathbf{N}} \end{bmatrix} [\mathbf{G}] dx dy \quad (3)$$

where $[\bar{\mathbf{N}}]$ is $\begin{bmatrix} N_x & N_{xy} \\ N_{xy} & N_y \end{bmatrix}$ and components of $[\mathbf{G}]$ are derivatives of shape functions with respect to natural coordinates of elements ζ_2 and ζ_3 .

By combined with a corotational method [18, 32], motions of structures subject to large displacements can be described. The detailed corotational shell finite element modeling can be found in the previous work of the authors [19]. The corotational method [18, 32] analyzes pure deformations of each finite element using the corotational frames by decoupling of the total element motion into a rigid body motion and a pure deformation. Figure 3 shows coordinate systems of the method for a general triangular shell element. The initial frame E_0 is defined with a transformation matrix \mathbf{T}_{E_0} relating the element coordinate in the undeformed state to the moving body frame built in the global frame G . Similarly, the current moving frame E is defined, and the corresponding transformation matrix is \mathbf{T}_E . A current position \mathbf{x}^B of a node can be obtained from the initial position \mathbf{X}^B in the body frame and a displacement of the node, \mathbf{u}^B . Triads S_0 and S are used to describe nodal rotations from the initial configuration to the current one in the body frame. A transformation matrix \mathbf{T} from the nodal triad S_0 to S in the current frame E is given by

$$\mathbf{T} = \mathbf{T}_E^T \mathbf{T}_S \mathbf{T}_{E_0} \quad (4)$$

where the transformation matrix \mathbf{T}_S which describes rotations of triad S in the body frame can be updated by assuming $\bar{\theta}_x$, $\bar{\theta}_y$, and $\bar{\theta}_z$ are the incremental rotations of triad S in the body frame [32]. Again, the detailed derivation of the transformation matrices can be found in Ref. [18, 19].

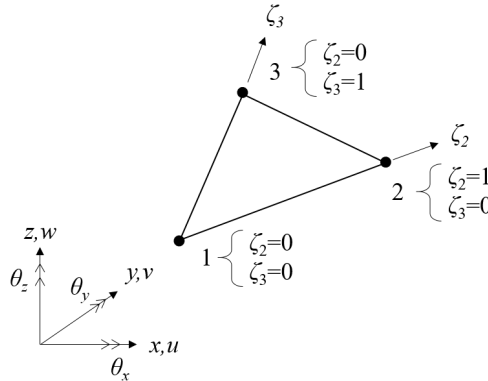


Figure 2. Geometry of the triangular element.

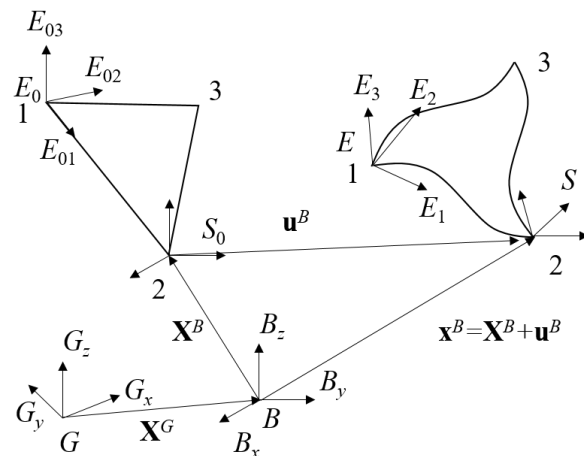


Figure 3. System frames of the triangular element.

B. Structural Model with 2-D HFS equation

The other nonlinear structural analysis is performed with 2-D flexible beam by solving HFS equation. Details of HFS equation can be found in Ref. [17, 33]. The formulation uses three coordinate systems as shown in Fig. 4 and assumes that shear stresses are negligible. The first coordinate (the a - c frame) is a rectangular coordinate system used as a reference frame. The second coordinate (the x - z frame) is an orthogonal curvilinear coordinate system having the x axis as the reference line penetrating the reference points of all cross sections of the original beam. The last coordinate (the ξ - ζ frame) is a local orthogonal curvilinear coordinate system. In the system, the ξ axis represents the deformed reference line and the ζ axis expresses the deformed z axis.

The constitutive relation is expressed as

$$\begin{Bmatrix} F_1 \\ M_2 \end{Bmatrix} = \mathbf{D} \begin{Bmatrix} e \\ \rho_2 - \kappa_2 \end{Bmatrix} \quad (5)$$

where F_1 and M_2 are the axial load and bending moment, \mathbf{D} is the bending stiffness, e , ρ_2 , and κ_2 are the strain at reference line, deformed curvature, and initial curvature, respectively.

2-D beam's HFS equations are given as

$$\begin{aligned}
F_1' &= -\rho_2 F_3 - T_{11} q_1 - T_{13} q_3 \\
F_3' &= \rho_2 F_1 + T_{13} q_1 - T_{11} q_3 \\
M_2' &= (1+e) F_3 - q_5 \\
T_{11}' &= \rho_2 T_{13} - T_{13} \kappa_2 \\
T_{13}' &= -\rho_2 T_{11} + T_{11} \kappa_2 \\
u' &= -1 - w \kappa_2 + (1+e) T_{11} \\
w' &= u \kappa_2 + (1+e) T_{13}
\end{aligned} \tag{6}$$

where F_3 is the shear load, q_1 , q_3 , and q_5 are the distributed axial and transverse loads and moments, T_{11} and T_{13} are components of the transformation matrix \mathbf{T} from the x - z frame to the ξ - ζ frame. These equations can be solved by multiple shooting method with the boundary condition:

$$At \quad s=0, \quad T_{11}=1, \quad T_{13}=u=w=0 \quad (7)$$

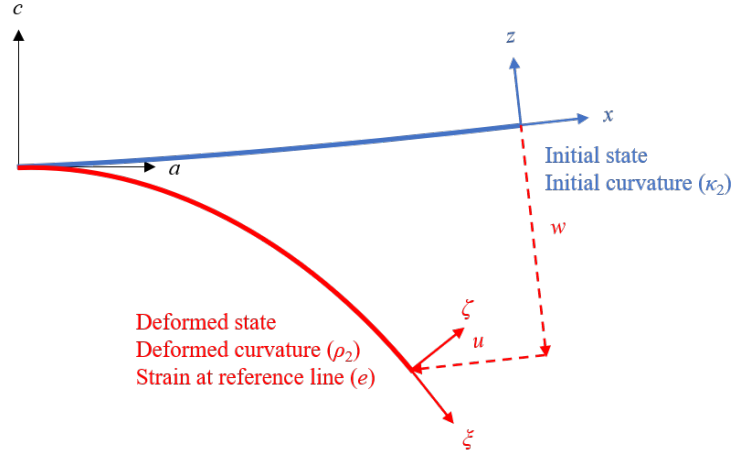


Figure 4. Definition of the coordinate systems used in the HFS equation.

C. 3-D Aerodynamic Model with Unsteady Vortex-Lattice Method

For the aerodynamic analysis, the unsteady vortex-lattice method (UVLM) [29] is used in the 3-D aeroelastic analysis. The UVLM assumes the velocity potential and applicable to incompressible flow. In the UVLM, lifting surfaces are modeled as a vortex singularity distribution on the discretized lifting surface panels using bound vortex rings as shown in Fig. 5. Front lines of bound vortex rings for each panel element are located at the quarter-chord position in a panel element, and the collocation points are at the center of the bound vortex rings. Influences of the wake convected from the TE is considered by shed vortex elements. The velocity potential of flow can be obtained from Laplace's equation which is

$$\nabla^2 \Phi = 0 \quad (8)$$

The boundary condition is zero normal flow across the wing surface, which can be written as

$$(\nabla \Phi_B + \nabla \Phi_w + \mathbf{v}) \cdot \mathbf{n} = 0 \quad (9)$$

where \mathbf{v} and \mathbf{n} are the lifting surface velocity and the normal vector to the lifting surface, and Φ_B and Φ_w are the potential of the bound elements and shed wake. In the time domain, the nonlinear unsteady kinematic motion of lifting surfaces under large displacements is taken into account through the kinematic velocity \mathbf{v} . In case of aeroelastic analysis in flight, the kinematic velocity \mathbf{v} includes the rigid body motion of aircraft \mathbf{v}_{RB} , wing vibration \mathbf{v}_{wing} , and additional external disturbance such as wind gust \mathbf{v}_{gust} :

$$\mathbf{v} = -(\mathbf{v}_{RB} + \mathbf{v}_{wing} - \mathbf{v}_{gust}) \quad (10)$$

By recalling the Biot-Savart law, the induced flow velocity \mathbf{w}_{ij} on the i^{th} bound vortex influenced by the j^{th} vortex ring is given as

$$\mathbf{w}_{ij} = \bar{\mathbf{w}}_{ij} \Gamma_j \quad (11)$$

where

$$\bar{\mathbf{w}}_{ij} = \sum_{k=1}^4 \left\{ \frac{1}{4\pi} \frac{\mathbf{r}_{mi} \times \mathbf{r}_{ni}}{|\mathbf{r}_{mi} \times \mathbf{r}_{ni}|^2} \mathbf{r}_{0i} \cdot \left(\frac{\mathbf{r}_{mi}}{r_{mi}} - \frac{\mathbf{r}_{ni}}{r_{ni}} \right) \right\}_k \quad (12)$$

where \mathbf{r}_{mi} , \mathbf{r}_{ni} , and \mathbf{r}_{0i} are position vectors of vortex ring corners on the i^{th} panel as defined in Ref. [29], and $m = 1, 2, 3, 4$ and $n = 2, 3, 4, 1$, which are the vortex ring corner nodes in clockwise order as shown in Fig. 5.

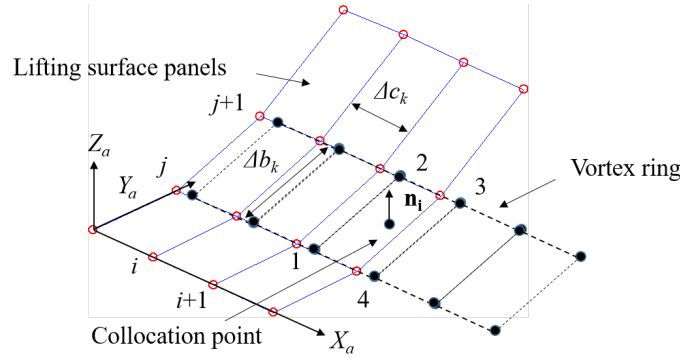


Figure 5. Vortex ring element on a lifting surface.

D. 2-D Aerodynamic Model for airfoils with XFOIL/UTCart

The aerodynamic analysis of 2-D airfoils is performed with two different solvers. The first solver is XFOIL, which is based on the panel method integrating viscous effect, in other words friction drag and flow separation [25]. The solver is cost-efficient and can easily obtain performance of airfoil. The second solver is a CFD code “UTCart” developed by Rinoie & Imamura Laboratory of the University of Tokyo [26-28, 34]. The full descriptions of the CFD code can be found in Refs. [26-28, 34]. The solutions of UTCart is based on the Reynolds Average Navier-Stokes (RANS) equations. Therefore, the 2-D aerodynamic solver is still cost-efficient, and it can also consider viscous effects and the stall.

E. Corrugated Panel Model

The equivalent properties of the periodically corrugated panel in one direction is calculated as a homogeneous orthotropic flat plate by considering the relation between the strain energies and the reaction forces and moments discussed in Ref. [35]. Adaptation of the model to the problem of aeroelastic analysis for a morphing wing with corrugated structure is implemented in the previous works [19]. A validation of the model has also been performed in the previous work. Figure 6 shows a periodic corrugated panel in one direction and the geometry of a round corrugation. Figure 6 shows two coordinate systems, the global and local frames, which are defined to calculate the corrugated panel properties. With the tangent and normal directions to the laminate, \tilde{t} and \tilde{n} , the local coordinate system is defined as shown in Fig. 6. The total thickness of the panel is t_p , and the thickness of the composite sheet forming the corrugation is \bar{t} .

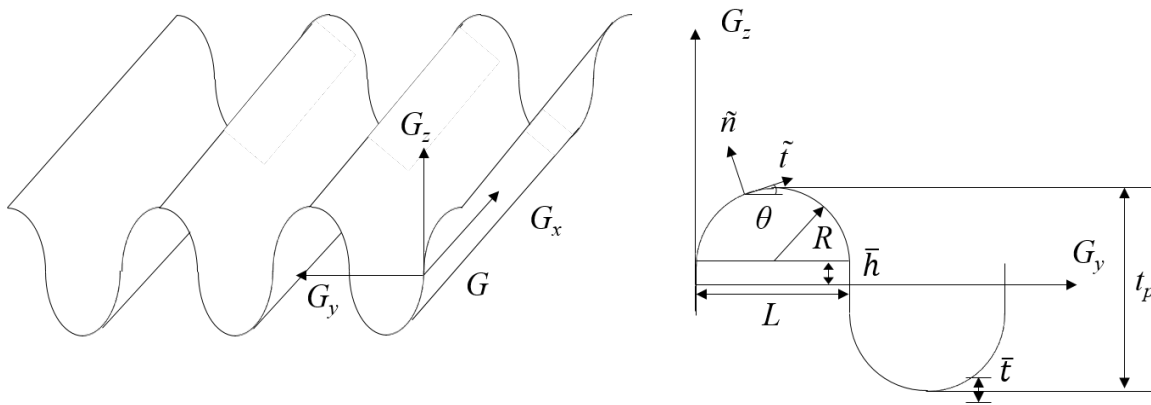


Figure 6. Definition of the corrugation coordinate systems.

By neglecting the coupling stiffness matrix \mathbf{B} , the constitutive relation of the equivalent orthotropic plate is

$$\begin{Bmatrix} \bar{N}_x \\ \bar{N}_y \\ \bar{N}_{xy} \\ \bar{M}_x \\ \bar{M}_y \\ \bar{M}_{xy} \end{Bmatrix} = \begin{bmatrix} \bar{A}_{11} & \bar{A}_{12} & 0 & 0 & 0 & 0 \\ \bar{A}_{12} & \bar{A}_{22} & 0 & 0 & 0 & 0 \\ 0 & 0 & \bar{A}_{66} & 0 & 0 & 0 \\ 0 & 0 & 0 & \bar{D}_{11} & \bar{D}_{12} & 0 \\ 0 & 0 & 0 & \bar{D}_{12} & \bar{D}_{22} & 0 \\ 0 & 0 & 0 & 0 & 0 & \bar{D}_{66} \end{bmatrix} \begin{Bmatrix} \bar{\epsilon}_x \\ \bar{\epsilon}_y \\ \bar{\gamma}_{xy} \\ \bar{\kappa}_x \\ \bar{\kappa}_y \\ \bar{\kappa}_{xy} \end{Bmatrix} \quad (13)$$

where $\bar{\epsilon}_x, \bar{\epsilon}_y, \bar{\gamma}_{xy}, \bar{\kappa}_x, \bar{\kappa}_y, \bar{\kappa}_{xy}$ are the strains and curvatures of the orthotropic plate at the mid-plane, and $\bar{N}_x, \bar{N}_y, \bar{N}_{xy}, \bar{M}_x, \bar{M}_y, \bar{M}_{xy}$ are the forces and moments. The properties \bar{A}_{ij} and \bar{D}_{ij} in Eq. (13) can be expressed as a function of the corrugation geometry. The equivalent stiffness properties of the orthotropic plate can be derived from a periodic Representative Volume Element. In the local coordinate (\bar{t}, \bar{n}, x) , the constitutive relation of the composite is

$$\begin{Bmatrix} N_t \\ N_x \\ N_{tx} \\ M_t \\ M_x \\ M_{tx} \end{Bmatrix} = \begin{bmatrix} A_{11} & A_{12} & 0 & 0 & 0 & 0 \\ A_{12} & A_{22} & 0 & 0 & 0 & 0 \\ 0 & 0 & A_{66} & 0 & 0 & 0 \\ 0 & 0 & 0 & D_{11} & D_{12} & 0 \\ 0 & 0 & 0 & D_{12} & D_{22} & 0 \\ 0 & 0 & 0 & 0 & 0 & D_{66} \end{bmatrix} \begin{Bmatrix} \epsilon_t \\ \epsilon_x \\ \gamma_{tx} \\ \kappa_t \\ \kappa_x \\ \kappa_{tx} \end{Bmatrix} \quad (14)$$

By following the homogenization approach in Ref. [35], equivalent stiffness components can be obtained as

$$\begin{aligned} \bar{A}_{11} &= \frac{\bar{A}_{12}A_{12}}{A_{22}} + \frac{s}{L} \frac{A_{11}A_{22} - A_{12}^2}{A_{22}}, \quad \bar{A}_{12} = \bar{A}_{21} = \frac{A_{12}}{A_{22}} \bar{A}_{22}, \quad \bar{A}_{22} = \frac{2L}{\frac{I_1}{A_{22}} + \frac{I_2}{D_{22}}}, \quad \bar{A}_{66} = \frac{L}{s} A_{66} \\ \bar{D}_{11} &= \frac{1}{2L} [A_{11}I_2 + D_{11}I_1], \quad \bar{D}_{12} = \bar{D}_{21} = \frac{D_{12}}{D_{22}} \bar{D}_{22}, \quad \bar{D}_{22} = \frac{L}{s} D_{22}, \quad \bar{D}_{66} = \frac{s}{L} D_{66} \end{aligned} \quad (15)$$

where

$$I_1 = \int_t \left(\frac{dy}{dt} \right)^2 dt, \quad I_2 = \int_t z^2 dt \quad (16)$$

and L and s are the half period and length of a corrugation. Here I_1 and I_2 are functions of the corrugation geometry obtained by Eq. (16). The equivalent Poisson's ratio is the same as that of the original composite forming the corrugated panel. In case of a round corrugation as shown in Fig. 6, $I_1 = \pi R$, $I_2 = 4\bar{h}^3/3 + 2\pi\bar{h}^2R + 8\bar{h}R^2 + \pi R^3$, $s = \pi R + 2\bar{h}$, and $L = 2R$. Therefore, the properties of corrugated panels can be controlled by the geometric parameters R and \bar{h} . On the other hand, if one wants to integrate corrugated structures into wings to achieve the morphing capability, the corrugation geometries have to be constrained by the original wing geometries. In other words, the geometric parameters R and \bar{h} should be determined based on the wing geometries as

$$R = \frac{1}{4} \left(\frac{\Delta c_{cor}}{n_{cor}} - 2\bar{t} \right), \quad \bar{h} = \frac{t_p}{2} - R \quad (17)$$

where Δ_{cor} is the element chord of corrugated panel, n_{cor} is the number of corrugation cycle, and t_p is the thickness between the wing's upper and lower surfaces.

Equivalent stiffness and bending stiffness of corrugate panel used for the HFS equations can be obtained in a similar manner. The full description can be found in Ref. [17].

F. Aero-Structure Interaction

In the present aeroelastic study, structural and aerodynamic calculations are performed with individual models in different coordinate systems. Therefore, a transformation between different analysis frames is required. In 3-D aeroelastic analysis, the aerodynamic mesh basically corresponds to the structural finite element mesh. Transformations from the aerodynamic loads on the collocation points to the structural grids on the shell finite elements and from structural deformation of all grids to aerodynamic meshes are performed with the Thin Plate Spline (TPS) [19]. Figure 7 describes the algorithm of the 3-D aeroelastic analysis framework. The analysis flow of the 2-D aeroelastic framework is described in Ref. [17].

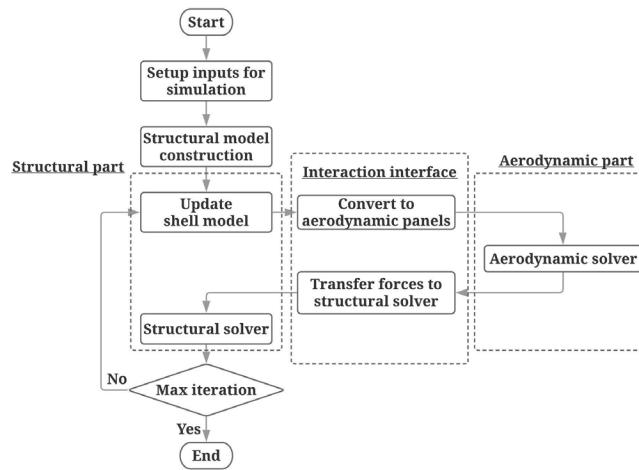


Figure 7. Algorithm of the 3-D aeroelastic analysis framework.

III. Numerical Studies

Computational differences in two different aeroelastic frameworks are evaluated in terms of accuracies for simulations of corrugated morphing wings. For the purpose, a series of simulations have been conducted to evaluate relative differences in the individual structural and aerodynamic models used in the different aeroelastic frameworks. In addition, the feasibility and capability of a morphing wing with a corrugated structure are demonstrated using the 3-D aeroelastic framework. The aeroelastic characteristics of the morphing wing are also evaluated.

A. Comparisons of Structural Analyses with Shell and Beam Models

In this paper, a morphing wing with a corrugated trailing-edge section replacing a traditional hinged flap is studied. In particular, differences in structural solutions of the two different analysis frameworks are evaluated in this section. Figure 8 shows the cross-sections of wings with a hinged flap and corrugated trailing-edge section. In the current study, it is assumed that the corrugated morphing section is closed by flexible skins to form the aerodynamic shape, and the stiffness of the skin is negligible. When the trailing-edge section is morphed, the wing chord is changed to the morphed chord that connects the leading edge and morphed trailing-edge.

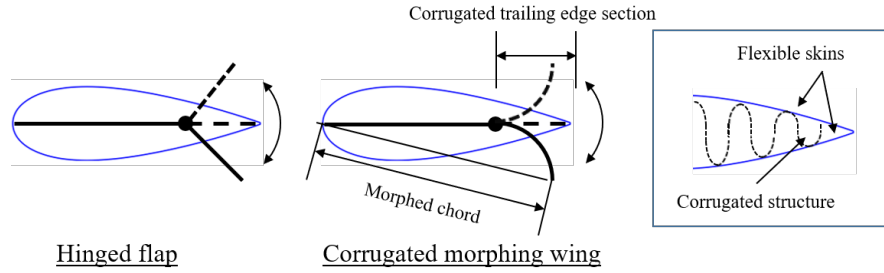


Figure 8. Cross-section of wings with a traditional hinged flap and corrugated trailing-edge section.

In the 2-D aeroelastic analysis framework, deformation shapes of a corrugated morphing wing are evaluated, focusing on a corrugated trailing-edge section. Structural simulations by the 2-D analysis are performed by modeling only a corrugated trailing-edge section as a chordwise beam, and the front edge of the trailing-edge section is fixed at a connection point to the main wing (a hinged point for a traditional hinged flap case). Therefore, the 3-D structural study is also performed by following the modeling method of the 2-D analysis framework.

1. Structural Simulations of Isotropic Cantilever Beam/Plate Subject to End Moment

A cantilever beam/plate made of an isotropic material subject to an end moment is studied. The geometry and material properties of the beam/plate is given in Table 1. An analysis model with shell elements is shown in Fig. 9. The shell model is discretized into 4 and 6 elements based on a convergence study. An end moment M of 10 kN·m is applied on the free edge in 10 steps. The vertical deflections at the free end of the shell and beam models obtained by the current framework and MSC.Nastran's nonlinear structural solver (SOL106) are given in Table 2. The solutions of the shell models are evaluated at free ends in the middle of the plate models. The nonlinear shell model has been validated for this bending analysis in the previous study [18, 19], and the errors between the solutions obtained by MSC.Nastran and HFS beam models to the shell model are 9% and 7.93%. The errors occur because the beam model ignores out-of-plane spanwise and in-plane shear deformations and stresses, which can be considered in the shell model. This simple comparison shows the fact that beam models overestimate chordwise bending deformations, which would describe a camber deformation in case of a camber morphing wing. Therefore, one has to be careful when beam models are used for camber morphing analysis.

Table 1. Geometry and material properties of the isotropic beam/plate.

Property	Value
Chordwise length, m	0.5
Spanwise length, m	0.5
Thickness, m	0.05
Young's modulus E , GPa	2.8
Poisson's ratio ν	0.4

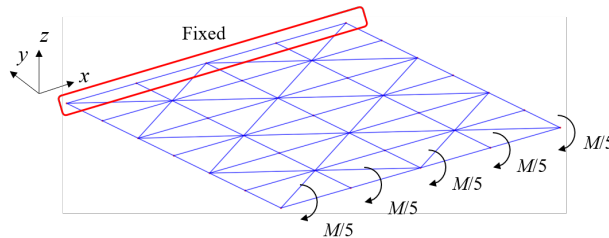


Figure 9. The isotropic cantilever plate subject to end moment.

Table 2. Vertical deflections of the isotropic beam/shell models at free end.

Property	Shell (Corotational)	Beam (Nastran)	Beam (HFS)
Vertical deflection, m	-0.07864	-0.08571	-0.084878
Error from shell to beam, %	-	9.00	7.93

2. Structural Simulations of Corrugated Composite Cantilever Beam/Plate Subject to End Moment

A composite cantilever beam/plate made of the orthotropic material, AS4/3501-6, subject to an end moment, is studied as a next step. The geometry and material properties of the beam/plate are given in Table 3. Two different aspect ratios, about 0.8 and 40, are evaluated. The analysis model with the aspect ratio close to 0.8 for shell elements is shown in Fig. 10. The shell model is discretized into 12 and 4 elements. An end moment M of 13 N-mm is applied on the free edge in 10 steps. The vertical deflections at the free end (on the middle of the plate for the plate model) obtained by the current frameworks are summarized in Table 4. The present shell model shows excellent agreement with the solution obtained by the HFS beam model when the aspect ratio is very small. On the other hand, when the aspect ratio is high, the error becomes larger since the beam model cannot consider out-of-plane spanwise and in-plane shear deformations and stresses, which is considered in the shell model.

Table 3. Geometry and material properties of the orthotropic beam/plate with AS4/3501-6.

Property	Value
Spanwise length, m	0.195/10
Chordwise length, m	0.48
Ply thickness, mm	0.127
Ply angles, deg	[90/0] _s
Axial modulus E_1 (GPa)	148
Transverse modulus E_2 (GPa)	10.5
Poisson's ratio ν_{12}	0.300
Poisson's ratio ν_{23}	0.590
Shear modulus G_{12} (GPa)	5.61
Shear modulus G_{23} (GPa)	3.17

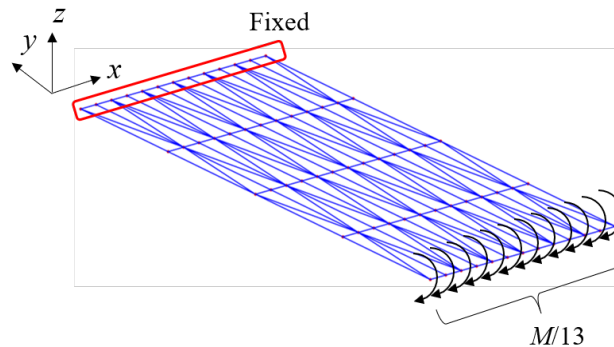


Figure 10. The composite cantilever plate subject to end moment with AR \approx 0.8.

Table 4. Vertical deflections of the composite beam/shell models with AR \approx 0.8 and 40.

Aspect ratio	Property	Shell (Corotational)	Beam (HFS)
0.8	Vertical deflection, mm	-5.345	-5.340
0.8	Error to the solution by the corotational shell, %	-	0.10
40	Vertical deflection, mm	-0.096145	-0.10413
40	Error to the solution by the corotational shell, %	-	8.30

Next, a cantilever beam/plate having round-corrugations constructed with the above-mentioned composite beam/plate is studied. Most of geometry, material properties, and finite discretization are the same as the composite laminate in the previous case, while the number of chordwise elements is changed to 10. The thickness of the corrugated structure is 12.51 mm, and the number of corrugations in each element n_{cor} is 4. The equivalent stiffness of the corrugated structure is calculated by the corrugated panel homogenization. An end moment M of 130 N-mm is applied on the free edge in 10 steps. The solutions of the corotational shell and HFS beam models are summarized in Table 6. The maximum vertical deflections at the free edge obtained by the shell and beam models are 133.61 mm and 133.59 mm. Angles between a horizontal line and another line connecting the front edge and trailing-edge (defined as “morphing angle” for a corrugated morphing wing in this study) are 16.39 deg. As corrugated structures are highly flexible in the corrugation direction, it can be observed that the structure undergoes the large deflection

even with the small moment compared with the original composite laminate constructing the corrugated structure. By taking advantage of this flexibility, a corrugated wing may achieve the morphing of the trailing-edge section with small required energy for actuation. However, due to the flexibility, a corrugated wing may also experience a roll-up of its trailing-edge section under aerodynamic loads in flight. Therefore, it is important to evaluate if such a roll-up of a trailing-edge section can be suppressed by an actuation mechanism while accomplishing wing morphing. A required force to achieve both objectives will also be studied in the following section.

Table 5. Geometry and structural properties of the corrugated beam/plate with the composite laminate.

Property	Value
Spanwise length, m	0.195
Chordwise length, m	0.48
Number of spanwise element	12
Number of chordwise element	10
Number of corrugations in each element	4
Axial modulus E_1 (GPa)	148
Transverse modulus E_2 (GPa)	10.5
Poisson's ratio ν_{12}	0.300
Poisson's ratio ν_{23}	0.590
Shear modulus G_{12} (GPa)	5.61
Shear modulus G_{23} (GPa)	3.17

Table 6. Vertical deflections of the corrugated beam/shell models.

Property	Shell (Corotational)	Beam (HFS)
Vertical deflection, mm	-133.61	-133.59
Error from shell to beam, %	-	0.02

B. Comparisons of Aerodynamic Analyses with UVLM and XFOIL/UTCart

For the correlation between the 2-D aerodynamic simulations with XFOIL or UTCart and the 3-D analysis with UVLM, solutions obtained by the different solvers are compared with different configurations. Mainly, a difference between the 2-D and 3-D aerodynamic analysis is caused by an influence of aspect ratio, which 2-D simulations cannot consider. When a lift/lift coefficient curve with different angles of attack is considered, a 3-D wing provides a smaller slope compared with a 2-D airfoil with the same airfoil profile due to the factor of aspect ratio. Therefore, only a high aspect ratio and slender wing can give a close result to a 2-D aerodynamic solution in the 3-D aerodynamic analysis. A suitable aspect ratio to perform effective comparisons of aeroelastic analyses for a corrugated morphing wing with different frameworks is explored in this section. For this study, thin rectangular wings with the semi-span of 0.5, 2, and 10 m and the chord of 0.5 m is used. The aspect ratios are 2, 10, and 40. Two different airfoils having NACA0012 and NACA2412 are tested to evaluate the effect of airfoil camber, which may also affect in a corrugated morphing wing. The flight conditions are altitude $h = 1,000$ m and Mach number $M = 0.1$.

1. Aerodynamic Simulations of Low Aspect Ratio Wing with Different Airfoil Profile

Firstly, 3-D aerodynamic solutions by UVLM with a low aspect ratio wing ($AR = 2$) are compared with 2-D solutions to confirm the influence of the aspect ratio. For UVLM simulations, an aerodynamic model is meshed into 10 and 20 panels in the spanwise and chordwise directions. The lift coefficients of NACA0012 and NACA2412 airfoils and low aspect ratio wings with the same airfoil profiles obtained by the different solvers are shown in Fig. 11. Since the XFOIL can solve both inviscid and viscous flow conditions, solutions with both conditions are plotted for comparison. It can be confirmed that the 3-D aerodynamic solutions for both NACA0012 and NACA2412 do provide lower lift curve slopes for both airfoil profiles. The difference in inviscid and viscous flow conditions is smaller than the difference in the 2-D and 3-D solutions, although the inviscid flow solutions provide slightly larger lift curve slopes. The simulations of XFOIL and UTCart with viscous flow conditions give almost the same lift coefficients for NACA0012 and NACA2412 airfoils (except over 3° for NACA2412).

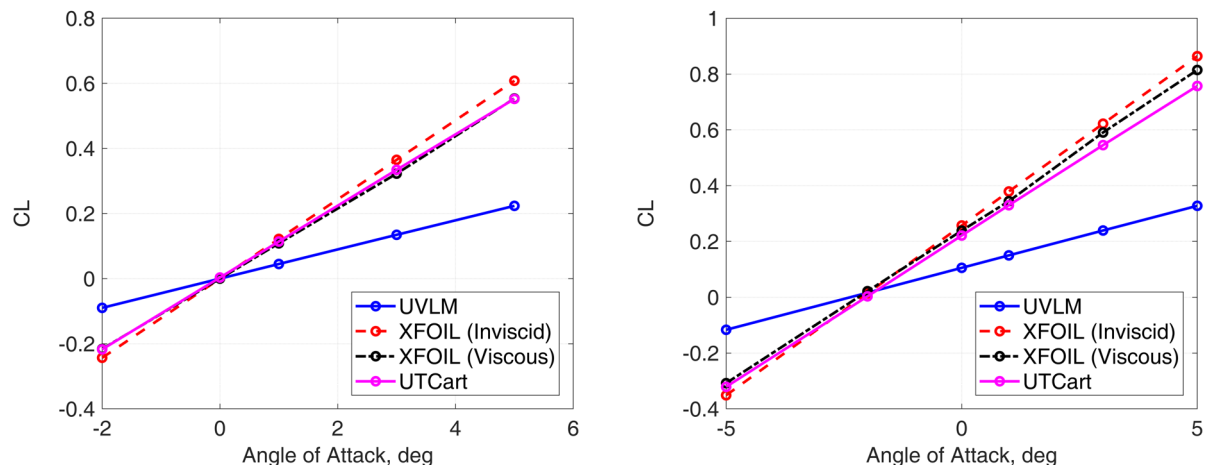


Figure 11. Lift coefficients of NACA0012 (left) and NACA2412 (right) airfoils and wings with $AR = 2$ at different angles of attack.

2. Aerodynamic Simulations of Higher Aspect Ratio Wing with Different Airfoil Profile

The lift coefficients of the two airfoils at different angles of attack are compared with the ones of higher aspect ratio wing ($AR = 10$ and 40). Figure 12 shows the comparisons of the lift coefficient curves with $AR = 10$. The lift curve slopes of the 3-D solutions get closer to the ones of the 2-D solutions. However, it is noted that the cambered airfoil provides larger differences in the XFOIL and 3-D solutions than the symmetric airfoil in the case of the higher aspect ratio wing. Table 7 lists the average errors of the lift coefficients between the solutions obtained from the different solvers with $AR = 10$, in which the solutions close to zero are omitted in the calculations of errors. Therefore, although 2-D aerodynamic models could be used for studies of morphing wings if their aspect ratios are sufficiently large, one needs to carefully evaluate the solutions, especially those of the morphing configurations. The lift coefficient curves with $AR = 40$ are shown in Fig. 13. The lift coefficients at different angles of attack obtained by the 3-D solution are much closer to the ones from the 2-D solutions. The average errors are less than when the airfoil is NACA0012. However, the errors are still almost 10% with the cambered airfoil in the solutions by XFOIL.

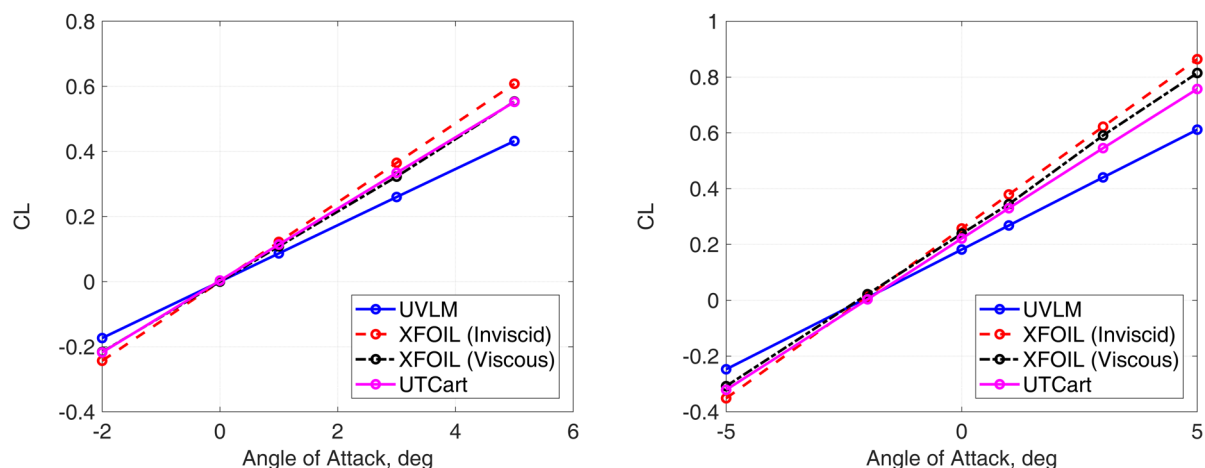


Figure 12. Lift coefficients of NACA0012 (left) and NACA2412 (right) airfoils and wings with $AR = 10$ at different angles of attack.

Table 7. Average errors of the lift coefficient calculations between different solvers with $AR = 10$.

Airfoil	XFOIL (inviscid) to UVLM	XFOIL (viscous) to UVLM	UTCart to UVLM
NACA0012	20.38%	13.12%	15.60%
NACA2412	24.71%	20.56%	12.54%

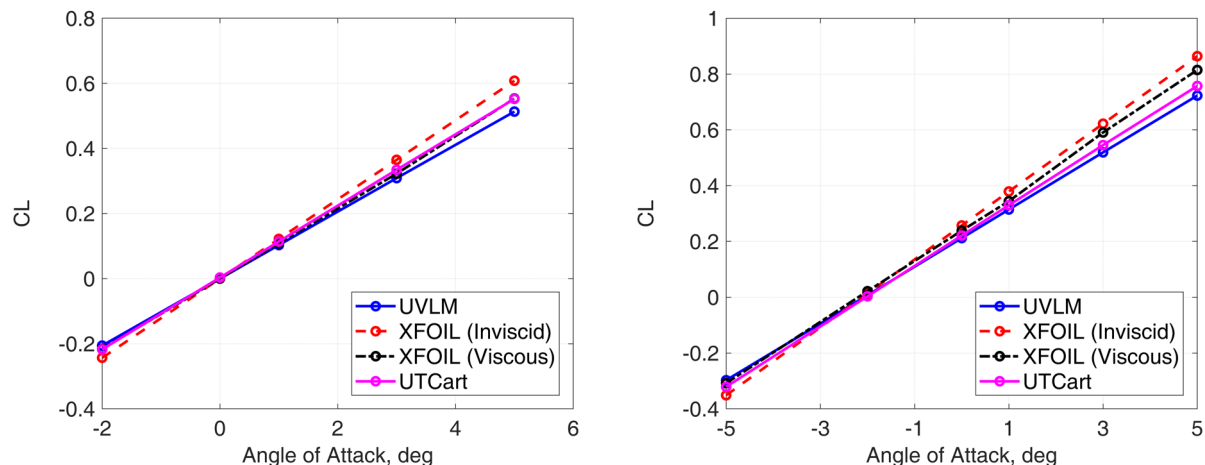


Figure 13. Lift coefficients of NACA0012 (left) and NACA2412 (right) airfoils and wings with $AR = 40$ at different angles of attack.

Table 8. Average errors of the lift coefficient calculations between different solvers with $AR = 40$.

Airfoil	XFOIL (inviscid) to UVLM	XFOIL (viscous) to UVLM	UTCart to UVLM
NACA0012	9.23%	3.12%	5.21%
NACA2412	12.59%	8.99%	2.19%

3. Aerodynamic Simulations of Camber Morphing Wing with Corrugated Trailing-Edge Section

The lift coefficients of the camber morphing wing with corrugated trailing-edge section at different angles of attack obtained by different aerodynamic solvers are evaluated and compared. The morphing shape obtained by the present shell finite element analysis in the previous section is used for the evaluation. For the purpose of modeling a whole wing, a main wing having the chord of 0.8 m is attached to the front edge of the corrugated trailing-edge section. In other words, the corrugated trailing-edge section starts from about 61.5% chord location (see Fig. 14). The chord length of the complete wing with the corrugated trailing-edge section in the morphed configuration is 1.3 m. Hence, the span is chosen to be 6.5 m so that the aspect ratio is close to 10 ($AR = 10.32$), which would make a difference in the 2-D and 3-D aerodynamic solutions smaller while maintaining a better aspect ratio for the structural analysis with the beam model. For 3-D aerodynamic panels are discretized into 12 and 26 elements in the spanwise and chordwise directions, respectively. The airfoil profile is NACA0012, and the chord line in the morphed configuration is aligned to the flow direction, which makes the effective angle of attack zero, as shown in Fig. 15. The flight altitude is 1,000 m, and the Mach number is 0.1. Table 9 shows the comparisons of the lift coefficients obtained by the different solvers for the corrugated morphing wing at the angle of attack of 0 deg. Since the solutions by XFOIL did not converge, only the 3-D solution by UVLM and the 2-D solution by UTCart are compared. It can be found that the errors in the lift coefficients of the morphing wing shape obtained by the UVLM and UTCart are not quite significant. Therefore, the simple 2-D analysis framework could provide aerodynamic characteristics of such morphing wings with corrugated structures if the aspect ratio is sufficiently large. However, both aeroelastic frameworks implement nonlinear structural algorithms, which involve numerical iterations. Consequently, the errors in the individual structural and aerodynamic calculations are accumulated in each iteration, influencing calculations in the next iteration mutually. As a result, considerable errors in the final solutions from the 2-D and 3-D aeroelastic simulations may occur. In order to avoid such large discrepancies, a 2-D aeroelastic framework should include the lift-curve slope correction with respect to the aspect ratio for the 3-D wing. However, the current 2-D analysis framework has not implemented the 3-D wing correction, and the implementation is in future works. Therefore, the following aeroelastic study is performed only using the 3-D analysis framework to demonstrate the capability of a camber morphing wing with a corrugated structure.

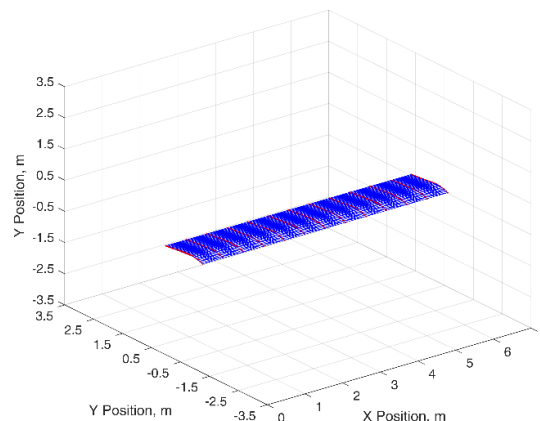
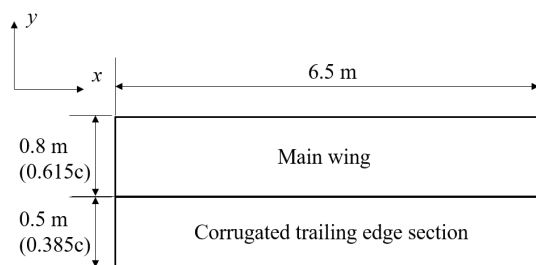


Figure 14. Planform (left) and finite element model (right) of the corrugated morphing wing.

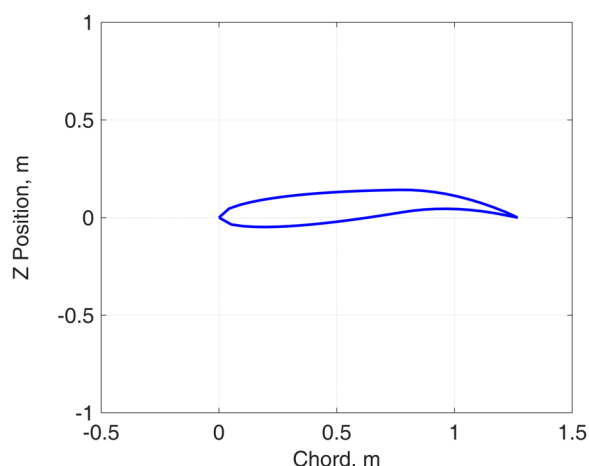


Figure 15. Cross-section of the complete wing in the morphed configuration.

Table 9. Lift coefficients obtained by different solvers with the corrugated morphing wing at angle of attack = 0 deg in the morphed configuration.

Property	UVLM	UTCart
CL	0.77559	0.81270
Error to UVLM, %	-	4.7844

C. Comparisons of Aeroelastic Analyses with Different Analysis Frameworks

Aeroelastic characteristics of a camber morphing wing with a corrugated trailing-edge section are studied using the 3-D analysis framework in this section. The design of a camber morphing wing with a corrugated trailing-edge section shown in Fig. 14 is used again. However, in this study, not only the wing shape but also structural properties are considered. The corrugated trailing-edge section is constructed with a composite laminate made of orthotropic material, AS4/3501-6. Table 10 lists the properties of the corrugated structure in the trailing-edge section and the composite laminate constructing the corrugated structure. In this study, it is assumed the main wing is sufficiently stiff as the simulations in the previous section.

Firstly, the load-bearing capability of the morphing wing is evaluated. For the aeroelastic simulation, the flight altitude is 1,000 m, the Mach number is 0.01, and the angle of attack is 0 deg. Cross-sectional shapes in the mid-span with the undeformed and deformed states are shown in Fig. 16. Corrugated structures exhibit flexibility in the corrugation direction, while they have high-stiffness in the transverse direction. Therefore, the out-of-plane spanwise bending of the trailing-edge section is minimal. In addition, it can be observed that the trailing-edge section is rolled up under the aerodynamic loads even at the very low free stream velocity. In other words, the bending stiffness in the chordwise direction is too low to sustain the aerodynamic loads at flight speed. Therefore, a

more stable design of a corrugated structure is modeled. The number of corrugations in an element is reduced from 4 to 1 so that the chordwise bending stiffness of the corrugated structure is increased. Figure 17 shows the camber shapes of the wing in the mid-span with $n_{cor} = 1$ at Mach number = 0.1. With $n_{cor} = 1$, the trailing-edge section could hold up to Mach number = 0.1 to start rolling up.

Table 10. Properties of the composite laminate with AS4/3501-6 and corrugated trailing-edge section.

Property	Value
Span, m	6.5
Chord (trailing-edge section), m	0.5
Laminate thickness, mm	4.064
Ply thickness, mm	0.127
Ply angles, deg	[90/0/90/0/90/0/90/0/90/0/90/0]s
Number of corrugations n_{cor}	4

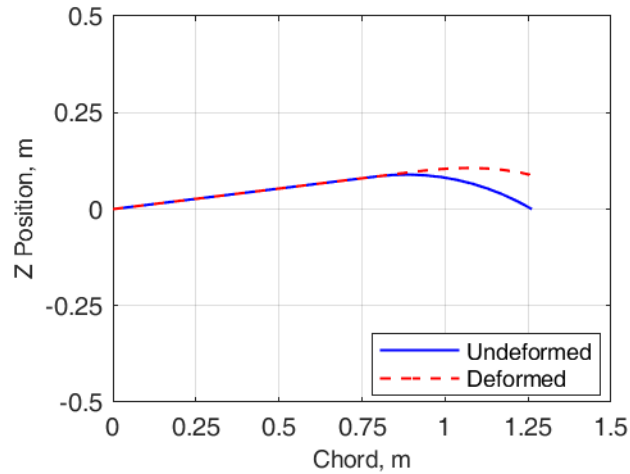


Figure 16. Deformed and undeformed camber shapes of the corrugated and morphed wing under aerodynamic loading with $n_{cor} = 4$ at Mach number = 0.01.

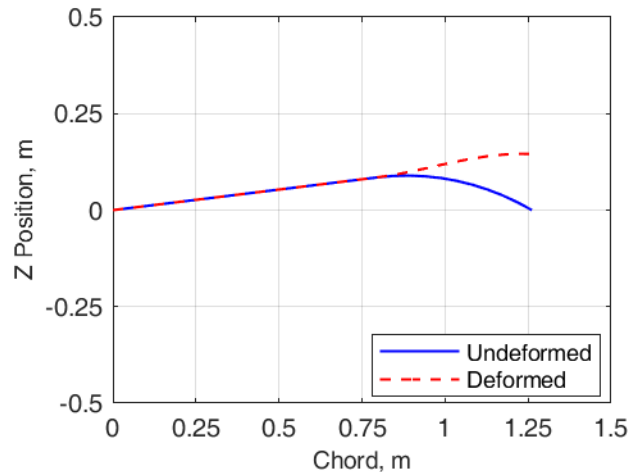


Figure 17. Deformed and undeformed camber shapes of the corrugated and morphed wing under aerodynamic loading with $n_{cor} = 1$ at Mach number = 0.1.

The capability to achieve wing morphing while preventing a roll-up of corrugated trailing-edge section under aerodynamic loads with an actuation mechanism is then evaluated. In this study, a simple actuation mechanism with wires and servomotors (see Fig. 18) is considered following the concept studied in Ref. [15], in which the feasibility of the actuation mechanism has been demonstrated in the wind tunnel test. The actuation is modeled as resultant

moments due to tensile loads of wires in simulations. The initial airfoil shape is considered as NACA0012 without any trailing-edge morphing. A 2.08-kN·mm actuation moment about the x -axis is applied at the 0.05-m location from the trailing-edge. The actuation moment is distributed on each node along the span in the shell finite element model. The flight conditions are an altitude of 1,000 m, a Mach number of 0.1, and an angle of attack of 0 deg. Figure 19 shows the camber shapes of the corrugated wing with the actuation under aerodynamic loads. Therefore, it was demonstrated that the corrugated morphing wing with the actuation mechanism could prevent the trailing-edge from rolling up and achieve camber morphing under the aerodynamic loads. Moreover, the morphing angle was 8.65 deg, and the camber morphing wing in the morphed configuration produced the lift coefficient of 0.707 even at the angle of attack = 0 with the symmetric airfoil.

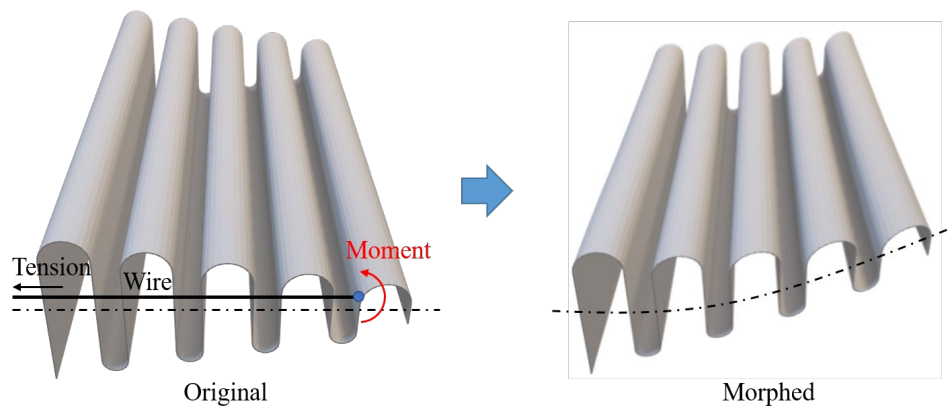


Figure 18. Actuation mechanism with wires and servomotors.

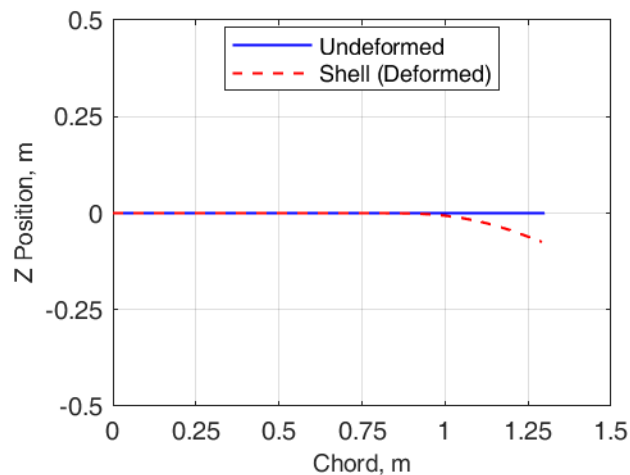


Figure 19. Deformed and undeformed camber shapes of the corrugated and morphed wing under aerodynamic and actuation loading.

IV. Conclusion

This paper presented two different aeroelastic formations for morphing wings providing different fidelities. One of the formulations used a 2-D beam's highly flexible structure (HFS) equation coupled with XFOIL or a CFD code "UTCart" developed by Rinoie & Imamura Laboratory of the University of Tokyo. The other coupled a co-rotational shell formulation with the UVLM to calculate aerodynamic loads. In both formulations, a homogenization method for corrugated structures was integrated into their structural models so that morphing wings with composite corrugated structures could be simulated. In addition, the numerical results obtained by the two aeroelastic

formulations were compared with respect to structural and aerodynamic characteristics. Finally, the feasibility and capability of a morphing wing with a corrugated structure were demonstrated using the 3-D aeroelastic framework. The aeroelastic characteristics of the morphing wing were also evaluated.

In the comparison of structural analyses, differences in structural solutions of the two different analysis frameworks were firstly evaluated. The simple comparison of structural simulations with the isotropic beam/plate models showed that beam models overestimated chordwise bending deformations, which would describe a camber deformation in case of a camber morphing wing. The structural solutions of beam and plate bending simulations with the composite laminates were also compared. There was an excellent agreement between solutions when the aspect ratios of the beam and plate models were very small. On the other hand, when the aspect ratio was high, the error of the beam model to the shell model became larger due to the simplification. In the structural study of the cantilever beam/plate having round-corrugations constructed with the composite beam/plate, it was observed that the structure experienced the large deflection even with the small moment compared with the original composite laminate constructing the corrugated structure. Therefore, it was confirmed that the corrugated wing could achieve the morphing of the trailing-edge section with the small required energy for actuation by taking advantage of this flexibility.

In the comparison of aerodynamic analyses, differences in the 2-D aerodynamic simulations with XFOIL or UTCart and the 3-D analysis with UVLM were evaluated. With the comparisons of solutions obtained by the different solvers, the influence of the aspect ratio on the lift coefficient curve slope was confirmed. When the aspect ratio was 40, the errors between the 2-D and 3-D solutions became less than 10% for NACA0012 and NACA2412 airfoil except for the inviscid solution of XFOIL for NACA2412 although such a large aspect ratio would produce a significant error in simulations with the beam model. The aerodynamic solutions of the corrugated morphing wing in the morphed configuration were also compared with the different solvers. XFOIL was failed to converge and could not provide any solutions for the case. It was found that the simple 2-D analysis framework with UTCart could provide sufficiently accurate aerodynamic characteristics of such morphing wings with corrugated structures if the aspect ratio was large enough. However, in the case of nonlinear structural algorithms involving numerical iterations, errors in the individual structural and aerodynamic calculations would be accumulated in each iteration, and considerable errors in the final solutions would occur. Therefore, the 2-D aeroelastic framework should include the lift-curve slope correction with respect to the aspect ratio for the 3-D wing in future work.

Aeroelastic characteristics of the designed camber morphing wing with the corrugated structure were evaluated by the 3-D analysis framework to demonstrate the capability of a camber morphing wing with a corrugated structure. With the properly designed corrugated structure, the trailing-edge section of the wing could achieve wing morphing while preventing a roll-up of corrugated trailing-edge section under aerodynamic loads with the simple actuation mechanism using wires and servomotors. Moreover, the morphing angle was 8.65 deg, and the camber morphing wing in the morphed configuration produced the lift coefficient of 0.707 even at the angle of attack = 0 with the symmetric airfoil.

Acknowledgements

This work was conducted under the financial support of Grant-in-Aid for Scientific Research (No.19K15216) by Japan Society for the Promotion of Science.

References

1. Pendleton, E., Flick, P., Paul, D., Voracek, D. F., Reichenbach, E., and Griffin, K., "The X-53 a Summary of the Active Aeroelastic Wing Flight Research Program," *48th AIAA/ASME/ASCE/AHS/ ASC Structures, Structural Dynamics and Materials Conference and Exhibit*, AIAA Paper 2007-1855, Honolulu, HI, Apr. 23-26, 2007.
2. Cumming, S. B., Smith, M. S., Ali, A., Bui, T. T., Ellsworth, J., and Garcia, C. A., "Aerodynamic Flight Test Results for the Adaptive Compliant Trailing Edge," *AIAA Atmospheric Flight Mechanics Conference*, AIAA Paper 2016-3855, Washington, DC, 2016.
3. Smith, M. S., Bui, T. T., Garcia, C. A., and Cumming, S. B., "Longitudinal Aerodynamic Modeling of the Adaptive Compliant Trailing Edge Flaps on a Giii Aircraft and Comparisons to Flight Data," *AIAA Atmospheric Flight Mechanics Conference*, AIAA Paper 2016-3703, Washington, DC, 2016.

4. Nguyen, N., Lebofsky, S., Ting, E., Kaul, U., Chaparro, D., and Urnes, J., "Development of Variable Camber Continuous Trailing Edge Flap for Performance Adaptive Aeroelastic Wing," *SAE 2015 AeroTech Congress and Exhibition*, SAE Technical Paper 2015-01-2565, Seattle, WA, Sep. 22-24, 2015.
5. Kaul, U. K., and Nguyen, N. T., "Drag Optimization Study of Variable Camber Continuous Trailing Edge Flap (VCCTEF) Using OVERFLOW," *32nd AIAA Applied Aerodynamics Conference*, AIAA Paper 2014-2444, Atlanta, GA, 2014.
6. Cooper, J. E., Chekkal, I., Cheung, R. C. M., Wales, C., Allen, N. J., Lawson, S., Peace, A. J., Cook, R., Standen, P., Hancock, S. D., and Carossa, G. M., "Design of a Morphing Wingtip," *Journal of Aircraft*, Vol. 52, No. 5, 2015, pp. 1394-1403.
7. Zhang, P., Zhou, L., Cheng, W., and Qiu, T., "Conceptual Design and Experimental Demonstration of a Distributedly Actuated Morphing Wing," *Journal of Aircraft*, Vol. 52, No. 2, 2014, pp. 452-461.
8. Vasista, S., Riemenschneider, J., van de Kamp, B., Monner, H. P., Cheung, R. C. M., Wales, C., and Cooper, J. E., "Evaluation of a Compliant Droop-Nose Morphing Wing Tip Via Experimental Tests," *Journal of Aircraft*, Vol. 54, No. 2, 2016, pp. 519-534.
9. De Gaspari, A., Riccobene, L., and Ricci, S., "Design, Manufacturing and Wind Tunnel Validation of a Morphing Compliant Wing," *Journal of Aircraft*, Vol. 55, No. 6, 2018, pp. 2313-2326.
10. Tsushima, N., and Su, W., "Concurrent Active Piezoelectric Control and Energy Harvesting of Highly Flexible Multifunctional Wings," *Journal of Aircraft*, Vol. 54, No. 2, 2016, pp. 724-736.
11. Tsushima, N., and Su, W., "Flutter Suppression for Highly Flexible Wings Using Passive and Active Piezoelectric Effects," *Aerospace Science and Technology*, Vol. 65, 2017, pp. 78-89.
12. Tsushima, N., and Su, W., "Modeling of Highly Flexible Multifunctional Wings for Energy Harvesting," *Journal of Aircraft*, Vol. 53, No. 4, 2016, pp. 1033-1044.
13. Ortiz, P., and Alley, N., "Spanwise Adaptive Wing-Ptera Flight Test," NASA AFRC-E-DAA-TN57887, 2018.
14. Takahashi, H., Yokozeki, T., and Hirano, Y., "Development of Variable Camber Wing with Morphing Leading and Trailing Sections Using Corrugated Structures," *Journal of Intelligent Material Systems and Structures*, Vol. 27, No. 20, 2016, pp. 2827-2836.
15. Yokozeki, T., Sugiura, A., and Hirano, Y., "Development of Variable Camber Morphing Airfoil Using Corrugated Structure," *Journal of Aircraft*, Vol. 51, No. 3, 2014, pp. 1023-1029.
16. Su, W., and Cesnik, C. E. S., "Strain-Based Geometrically Nonlinear Beam Formulation for Modeling Very Flexible Aircraft," *International Journal of Solids and Structures*, Vol. 48, No. 16-17, 2011, pp. 2349-2360.
17. Sato, K., and Yokozeki, T., "Aero-Structural Evaluation of Morphing Control Surface Using Corrugated Panels," *Transactions of the Japan Society for Aeronautical and Space Sciences*, Vol. 15, APISAT-2016, 2017, pp. a7-a15.
18. Khosravi, P., Ganesan, R., and Sedaghati, R., "Corotational Non-Linear Analysis of Thin Plates and Shells Using a New Shell Element," *International Journal for Numerical Methods in Engineering*, Vol. 69, No. 4, 2007, pp. 859-885.
19. Tsushima, N., Yokozeki, T., Su, W., and Arizono, H., "Geometrically Nonlinear Static Aeroelastic Analysis of Composite Morphing Wing with Corrugated Structures," *Aerospace Science and Technology*, Vol. 88, 2019, pp. 244-257.
20. Jung, Y. S., Yu, D. O., and Kwon, O. J., "Aeroelastic Analysis of High-Aspect-Ratio Wings Using a Coupled Cfd-Csd Method," *Transactions of the Japan Society for Aeronautical and Space Sciences*, Vol. 59, No. 3, 2016, pp. 123-133.
21. Chimakurthi, S. K., Stanford, B. K., Cesnik, C. E., and Shyy, W., "Flapping Wing Cfd/Csd Aeroelastic Formulation Based on a Corotational Shell Finite Element," *50th AIAA/ASME/ASCE/AHS/ASC Structures, Structural Dynamics, and Materials Conference*, AIAA Paper 2009-2412, Palm Springs, CA, 2009.
22. de Souza, C., da Silva, R. G., and Cesnik, C., "Nonlinear Aeroelastic Framework Based on Vortex-Lattice Method and Corotational Shell Finite Element," *53rd AIAA/ASME/ASCE/AHS/ASC Structures, Structural Dynamics and Materials Conference*, AIAA Paper 2012-1976, Honolulu, HI, Apr. 23-26, 2012.
23. Su, W., Huang, Y., and Hammerton, J. R., "Nonlinear Aeroelasticity of Highly Flexible Joined-Wing Aircraft Using Unsteady Vortex-Lattice Method," *58th AIAA/ASCE/AHS/ASC Structures, Structural Dynamics, and Materials Conference*, AIAA Paper 2017-1353, Grapevine, TX, 2017.
24. Soneda, K., Yokozeki, T., and Imamura, T., "Study of Aero-Structural Model of Camber Morphing Wing Using Corrugated Panels," *56th Aircraft Symposium*, Yamagata, Japan, Nov. 14-16, 2018 (in Japanese).

25. Drela, M., "XFOIL: An Analysis and Design System for Low Reynolds Number Airfoils," Berlin, Germany, 1989.
26. Takahashi, Y., and Imamura, T., "Steady Flow Simulation Using Immersed Boundary Method and Wall Function Based on Sa Turbulence Model," *27th Computational Fluid Dynamics Symposium* Nagoya University, 2013.
27. Tamaki, Y., Harada, M., and Imamura, T., "Near-Wall Modification of Spalart–Allmaras Turbulence Model for Immersed Boundary Method," *AIAA Journal*, Vol. 55, No. 9, 2017, pp. 3027-3039.
28. Tamaki, Y., and Imamura, T., "Turbulent Flow Simulations of the Common Research Model Using Immersed Boundary Method," *AIAA Journal*, Vol. 56, No. 6, 2018, pp. 2271-2282.
29. Katz, J., and Plotkin, A., *Low-Speed Aerodynamics*, Cambridge University Press, Cambridge, UK, 2001.
30. Felippa, C. A., "A Study of Optimal Membrane Triangles with Drilling Freedoms," *Computer Methods in Applied Mechanics and Engineering*, Vol. 192, No. 16-18, 2003, pp. 2125-2168.
31. Batoz, J. L., Bathe, K. J., and Ho, L. W., "A Study of Three-Node Triangular Plate Bending Elements," *International Journal for Numerical Methods in Engineering*, Vol. 15, No. 12, 1980, pp. 1771-1812.
32. Rankin, C., and Brogan, F., "An Element Independent Corotational Procedure for the Treatment of Large Rotations," *Journal of pressure vessel technology*, Vol. 108, No. 2, 1986, pp. 165-174.
33. Pai, P. F., *Highly Flexible Structures: Modeling, Computation, and Experimentation*, American Institute of Aeronautics and Astronautics, 2007.
34. Imamura, T., Tamaki, Y., and Harada, M., "Parallelization of a Compressible Flow Solver (Ucart) on Cell-Based Refinement Cartesian Grid with Immersed Boundary Method," *29th International Conference on Parallel Computational Fluid Dynamics* Glasgow, UK, 2017.
35. Xia, Y., Friswell, M. I., and Flores, E. I. S., "Equivalent Models of Corrugated Panels," *International Journal of Solids and Structures*, Vol. 49, No. 13, 2012, pp. 1453-1462.